Chapter 4. Microwave Scattering from the Sea

Donald R. Thompson
Johns Hopkins University Applied Physics Laboratory, Laurel, Maryland USA

4.1 Introduction

There is at present considerable interest in achieving a better understanding of the physics that governs the scattering of microwave radiation from the sea. This interest is due in large part to the rapid advances in ocean remote sensing using microwave techniques during the past two decades or so. These advances were triggered by the extremely rich and varied data sets collected by microwave sensors on numerous spaceborne satellite missions undertaken during this period. The microwave instrumentation flown on these missions included synthetic aperture radar (SAR), wind scatterometers, and altimeters. Additional missions with advanced microwave sensors are planned for launch in the near future. As these missions proceed and analysis of the data progresses, the operational use of microwave radar for the estimation of useful geophysical parameters should become possible.

In order to extract geophysical information from the data collected by microwave sensors, it is clear that one must understand not only the scattering physics, but also surface wave hydrodynamics and the structure of the marine boundary layer. In particular, a method for characterizing the shape of the sea surface (and perhaps even its evolution) is necessary in order to properly apply the electromagnetic boundary conditions. A convenient way to proceed with this characterization is through the surface-height spectral density. Thus, we begin this chapter by presenting a general description of rough-surface scattering based on knowledge of the surface spectrum. This description will motivate the more general discussion of spectral modulation by wind fluctuations and spatially varying current fields that follows.

4.2 Background

Perhaps the most common example of electromagnetic scattering is that from a completely flat horizontal interface between free space and another medium with relative dielectric constant ε_r and relative permeability μ_r. (For conducting media such as the ocean, ε_r is a complex number whose imaginary part is related to the conductivity, and for most common materials, μ_r is of order unity.) It is a standard problem in electrodynamics to apply the boundary conditions on the electric and magnetic fields at the interface to obtain the Fresnel reflection and transmission coefficients [e.g., *Jackson*, 1997]. As expected, one finds that a portion of the incident field is reflected at the interface in the plane defined by the incident wavenumber and the surface normal vector (called the plane of incidence) along a direction such that the angle of reflection equals the angle of incidence (like an ordinary mirror). This process is sometimes called "specular reflection." The remaining portion of the incident field is transmitted into the medium (also in the plane of incidence) along a direction defined by the familiar Snell's law. A schematic of the situation is shown in Figure 4.1. The top panel shows the case when the incident electric field is in the plane of incidence, while in the bottom panel, the incident *E* field is perpendicular to the incident plane. The former case is commonly referred to as vertical polarization, the latter is horizontal polarization. The Fresnel coefficients are generally different for the two cases. Note that for both cases, the directions of the electric field vector ($\vec{E}$), the

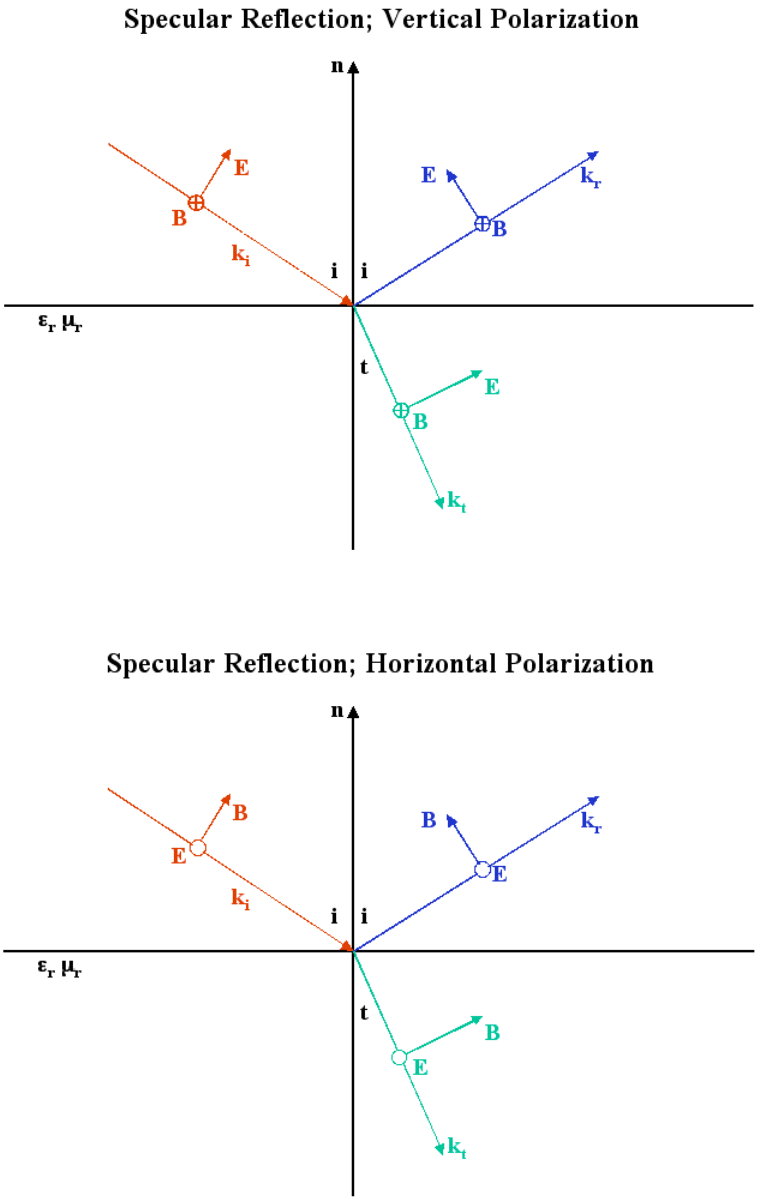

Figure 4.1. Reflection and refraction from a plane interface where the lower medium has relative dielectric constant ε_r and relative permeability μ_r. The top panel shows the field orientation when the incident electric field is in the plane of incidence (Vertical Polarization). In the bottom panel, the *E* field is perpendicular to (directed into) the plane of incidence (Horizontal Polarization).

magnetic field vector ($\vec{B}$), and the direction of propagation ($\vec{k}$) are mutually orthogonal and satisfy the relation $\hat{E} \times \hat{B} = \hat{k}$. The strength of the transmitted field is attenuated as it penetrates into a conducting medium. For sea water, the "skin depth" (distance where the intensity falls to e^{-1} of its initial value) of microwave radiation is about 0.4 cm for a frequency of 1 GHz (30-cm wavelength) and 0.1 cm for 10 GHz (3-cm wavelength). For a perfect conductor, there is no penetration into the medium, and all the incident energy is reflected from the interface for both polarization states regardless of the angle of incidence.

As seen above for the special case of a smooth flat surface, the incident energy is reflected into the specular direction (or dissipated in the medium). Thus a monostatic radar system, which transmits and receives using a single antenna, will receive no (backscattered) signal from such a surface. The sea surface, of course, is not smooth and flat. Its roughness spectrum can span scales covering more than five decades; from several hundred-meter swell waves, through wind-generated waves with wavelengths ranging from several tens of meters to a centimeter or so, to short capillary waves with wavelengths of only a few millimeters. Since the root-mean-square (rms) slope of the sea surface is generally small, most incident electromagnetic radiation is still scattered in the specular direction. The presence of the surface roughness however causes a small amount of the incident radiation to be scattered into all other directions; in particular back toward the transmitting antenna (in the backscatter direction).

An accurate description of microwave scattering from the sea is therefore considerably more complicated than for the case of the smooth flat interface discussed above. In particular, the complicated nature of the sea-surface roughness spectrum renders proper application of the electromagnetic boundary conditions quite difficult. We turn our attention now to a discussion of methods for handling this rough surface scattering problem and implications of these methods on the interpretation of microwave remote-sensing data.

4.3 Scattering from a Rough Surface

All available closed-form models for electromagnetic scattering from rough surfaces are asymptotic approximations to an exact solution of Maxwell's equations. The two most commonly used models are the Kirchhoff approximation [*Beckmann and Spizzichino*, 1963] and the small perturbation method (SPM) [*Ulaby et al*., 1982]. The Kirchhoff approximation is valid for small slopes and long wavelengths. It correctly models quasi-specular scattering, but lacks polarization sensitivity. The SPM is valid for small slopes and short wavelengths. It yields the proper polarization sensitivity for this regime, but does not properly account for long-scale features in the surface spectrum and does not account for specular scattering. Recently, a popular approach has been to investigate successive iterations of the so-called surface-current integral equation in order to find a model that is correct for both of the above limits. In fact, several authors have found relatively simple closed-form expressions for the scattered field that satisfy this criterion. For detailed discussion of these scattering models and interaction of the surface-current integral equation, see for example: *Voronovich* [1994], *Fung*, [1994], and *Elfouhaily et al.* [1999, 2001a], and references contained therein.

4.3.1 Analytical Model

To continue our general discussion of backscatter from the sea in this chapter, we will assume for simplicity that the ocean is a perfect conductor and utilize the scattering model developed by *Elfouhaily et al.* [1999, 2001a]. In the context of this model, the scattered (magnetic) field, $B_s^p(r)$, at the field point r resulting from a plane-wave incident field is given by

$$\vec{B}_s^{\,p}(r) = \frac{1}{2p\,i}\frac{e^{ikr}}{r} B_0 \vec{P}_s^{\,p} \int_R \exp\left[-iq_z h(\vec{x})\right] \exp\left[-i\vec{q}_H \cdot \vec{x}\right] d\vec{x} \tag{1}$$

where B_0 is the magnitude of the incident field, $\vec{P}_s^p$ is a polarization vector that describes the scattered field for incident polarization state p, and $h(\vec{x})$ is the surface elevation (above the mean level) at position $\vec{x}$. The vector $\vec{P}_s^p$ has the form

$$\vec{P}_s^p = \left\{ \frac{\vec{q}}{q_z} \times \hat{P}_i^p + 2\left(\frac{\vec{q}}{q_z} \cdot \hat{P}_H \right) \vec{Q}_H - \left(\frac{\vec{q}}{q_z} \cdot \frac{\vec{k}_H^s + \vec{k}_H^i}{q_z} \right) \hat{P}_H \right\} \times \frac{\vec{k}_s}{k} \tag{2}$$

with $\hat{P}_i^p$ being the polarization of the incident field, $\hat{P}_H = \hat{e}_z \times \hat{P}_i^p$, and

$$\vec{Q}_H = \frac{1}{2} \frac{\vec{k}_H^s + \vec{k}_H^i}{k_z^s + k_z^i} \tag{3}$$

Also in (1), (2), and (3), $\vec{k}^s$ and $\vec{k}^i$ are the scattered and incident wavenumber vectors, respectively, with horizontal and vertical components indicated by the subscripts H and z. The vector $\vec{q}$ is the difference between the scattered and incident wavenumber vectors with the same meaning for the subscripts H and z. Finally, the indices i and s denote incident and scattered fields, respectively, while the indices p and q denote respectively the incident and scattered polarization states.

The normalized radar cross section (NRCS), s^0_{pq}, described by (1) and corresponding to the component of the scattered field with polarization $\hat{P}_s^q$ when the incident field has polarization $\hat{P}_i^p$ is given by

$$s^0_{pq} = \lim_{r \to \infty} \frac{4pr^2}{A} \frac{\left\langle \vec{B}_s(r) \vec{B}_s(r)^* \right\rangle}{B_0^2} \tag{4}$$

where A is the illuminated area on the horizontal surface, $\langle \bullet \rangle$ represents ensemble averaging, and the scattered field is given by (1).

The bistatic scattering model specified by (1), (2), and (3) has been compared against an exact numerical solution of Maxwell's equations for microwave scattering from a random ocean surface with broadband roughness spectrum characteristic of the ocean as discussed qualitatively above. Results of this comparison for 0.1-m radiation (S-band) from a 1-dimensional random surface with roughness scales corresponding to a 10 m s^{-1} wind speed are shown for vertical and horizontal polarization in the upper and lower panels of Figure 4.2, respectively. The values shown in the figure are the average NRCS computed from 50 surface realizations. Positive angles indicate forward scattering, while negative angles represent scattering toward the quadrant where the radar transmitter is located. The angle of incidence was -30° for both polarizations. One can see from Figure 4.2 that for both polarization states, the scattered intensity is maximum at 30° which corresponds to the specular direction, but that scattered intensity is present at all directions including the backscatter direction of -30°. Note that the blue diamonds corresponding to the new bistatic model described above agree quite well for both polarizations with the red crosses that represent the results of an exact numerical computation using the multi-grid iterative approach (MGIA) for scattering angles whose magnitude is less than about 50°.

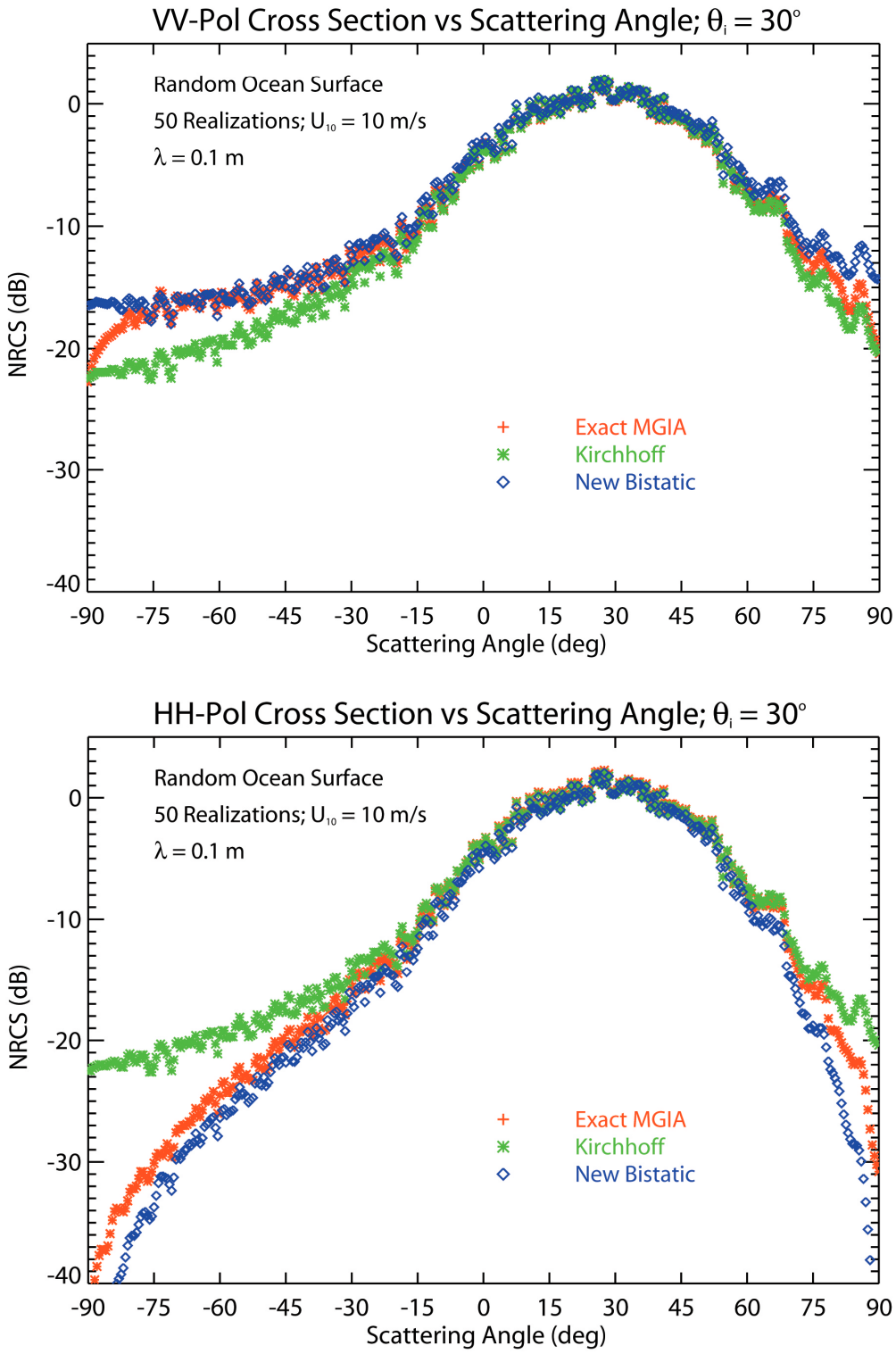

Figure 4.2. Bistatic NRCS for scattering of 0.1 m wavelength radiation from a simulated 1-D random ocean surface corresponding to a 10 m s^{-1} wind speed. The red crosses indicate the NRCS from an exact numerical computation (MGIA), the green asterisks show the Kirchhoff values, and the blue diamonds give the results of the analytical bistatic model. The top panel shows the results for vertical polarization, while horizontal polarization is shown in the bottom panel.

(For a discussion of the MGIA, see e.g. the article by Donohue, *et al*. in Brown, [1998].) For angles greater than this, the HH-pol predictions are slightly low. The Kirchhoff cross section (green asterisks) is the same for both polarization states, and is lower than the exact results at VV-pol and higher than those for HH-pol. More details of the calculations and the comparisons shown in Figure 4.2 may be found in *Elfouhaily et al.* [2001a].

4.3.2 Scattering from the Sea Surface in the SPM (Bragg) Limit

Given the general validity of the analytical model for the bistatic scattered field discussed in the previous sub-section, we may now use this model to examine how the measured NRCS is related to the properties of the sea surface itself. Understanding of such relationships forms the basis of ocean remote sensing. To begin, we look at the form of the scattered field given by (1) when the rms surface height is small compared to the microwave wavelength; the small perturbation method (SPM) or Bragg scattering limit.

To find the form of (1) in the SPM limit, we may simply expand the phase factor involving the surface height in the integrand to obtain

$$\vec{B}^{p}_{sspm}(r) = \frac{1}{2pi}\frac{e^{ikr}}{r} B_0 \vec{P}_s^{\,p} \int_R \left\{1 - iq_z h(\vec{x})\right\} \exp\left[-i\vec{q}_H \cdot \vec{x}\right] d\vec{x} \tag{5}$$

This expression may now be substituted into (4) to find the corresponding cross section, s_{pq}^{SPM} to be

$$s_{pq}^{SPM} = \frac{k^2}{p}\frac{\left|\hat{P}_s^{q} \cdot \vec{P}_s^{\,p}\right|^2}{A} \iint_R \exp\left[-i\vec{q}_H \cdot (\vec{x} - \vec{x}')\right]\left\{1 + q_z^2 \left\langle h(\vec{x}) h(\vec{x}')\right\rangle\right\} \mathrm{d}\vec{\mathrm{x}}\, \mathrm{d}\vec{\mathrm{x}}' \tag{6}$$

where $\hat{P}_s^q$ describes the polarization of the scattered field. The ensemble average in (6) is simply the surface autocorrelation function. If the scattering surface, $h(\vec{x})$, can be described in terms of a two-point correlated Gaussian random process, then the autocorrelation function, $f(\vec{x} - \vec{x}')$, is a function only of the difference vector $\vec{x} - \vec{x}'$. Recognizing that the Fourier transform of the (symmetrized) surface spectrum $y\left(\vec{k}\right)$ is the autocorrelation function, we may write the cross section in the SPM limit as

$$s_{pq}^{SPM} = 4pk^2 \left|\hat{P}_s^q \cdot \vec{P}_s^{\,p}\right|^2 \left\{d\left(\vec{q}_H\right) + \frac{1}{2}\left[y\left(\vec{q}_z\right) + y\left(-\vec{q}_z\right)\right]\right\} \tag{7}$$

The first term in this expression involving the Dirac δ-function represents specular scattering, and contributes only when $\vec{q}_H$ is zero; that is when $\vec{k}_s^{\,H} = \vec{k}_i^{\,H}$ so that the angle of incidence equals the angle of reflection as we found earlier in the simple example of a mirror-like surface. Since we will be primarily concerned with backscattering geometry in the following discussion, we can further simplify (7) to this geometry by recalling that for backscattering, $\vec{k}_s = -\vec{k}_i$. With

this simplification and the substitutions $q_s = q_i \equiv q$, we finally arrive at the desired expression, s_{pq}^{BSPM}, for the backscatter NRCS in the SPM limit

$$s_{pq}^{BSPM} = 4pk^2 d\left(2\vec{k}_H\right) + 8pk^4 \left|G_s^{pp}(q)\right|^2 \left[y\left(2\vec{k}_H\right) + y\left(-2\vec{k}_H\right)\right] \tag{8}$$

where $\left|G_s^{pp}(q)\right|^2$ represents the dot product of the polarization vectors in (7) evaluated for backscatter geometry, and takes the form

$$\left|G_s^{pp}(q)\right|^2 = \begin{cases} \left(1+\sin^2 q\right)^2 & \text{for } pp = \text{VV - pol} \\ \cos^4 q & \text{for } pp = \text{HH - pol.} \end{cases} \tag{9}$$

Note that for backscatter geometry, the specular term in (8) contributes only at nadir (q=0°). One can also see that an important parameter in (8) is twice the projection of the radar wavenumber vector on the horizontal surface. This quantity, $2\vec{k}_H (= 2k\sin q)$, is known as the Bragg wavenumber, and in the SPM limit it probes different components of the surface wave spectrum as the incident angle q varies. Finally, we have included only like polarization states, *pp*, in (8) and (9) since for the SPM, the de-polarization NRCS is zero.

At this point, the reader may wonder why we have bothered to examine the SPM limit of (1), (2), and (3) since, except for very light wind conditions, the rms surface height of the sea surface is considerably larger than the radar wavelength, and the SPM conditions are not generally valid. The reason for the examination of the SPM is that the dependence of the NRCS on the properties of surface waves, not readily apparent in (1), (2), and (3), is more easily appreciated in this limit. We should mention here that a model which includes the effects of longer surface waves may be explicitly developed in a manner similar to that used for the SPM above by dividing the surface spectrum into long and short waves. This yields the so-called two-scale or composite model. (For a review of this development in particular and the composite model in general, see *Thompson*, 1989; *Plant*, 1991, and references contained therein.) The form of the composite-model expression for the backscatter NRCS is similar to (8) except that the small-scale waves now propagate on a "wavy" long-scale surface instead of a flat one. The presence of the long-wave surface effectively modulates the local incident angle. This modulation broadens the angular region (around q=0°) where specular scattering is important, and also changes the Bragg wavenumber as a function of position along the long-wave surface. In particular in the composite model, the long-wave slope moments affect the NRCS as well as the local Bragg spectral components. We will have more to say about the composite model in Section 4.3.5. The point we want to emphasize here is that the 2-dimensional properties of the sea surface (i.e., the magnitude and direction of the 2-D surface wave spectrum) determine the characteristics of the measured NRCS. Now that we've motivated this dependence using the SPM through (8), we turn to a discussion of the properties of the surface wave spectrum and how they depend on environmental parameters such as the local wind vector.

4.3.3 Properties of the Ocean Surface Wave Spectrum

Precise specification of a 2-D function whose value is the surface height at every point contained inside the footprint of a microwave radar at a given instant in time is extremely

challenging. This is not only because of the broad range of roughness scales present on the sea surface, but also because such an area extensive measurement usually requires complicated optical and photographic systems that are themselves difficult to calibrate. Most routine measurements of the sea surface are limited to the height and directional characteristics of the wave field collected from a wave buoy at a single position in space as a function of time. There are many studies in the recent literature that discuss how to assimilate such measurements into models for the sea-surface wave spectra. (e.g., *Phillips* [1977] or *Komen et al*., [1994] and references contained therein.) These models generally characterize the measured properties of the sea surface through the spectral moments. Also as we have seen above, concise analytical formulation of the models is important for remote sensing applications.

A few of the more popular spectral models are those of *Bjerkaas and Riedel* [1979], *Donelan and Pierson* [1987], *Apel* [1994], and *Elfouhaily et al*., [1997]. For our general discussion here, we choose the spectral model of *Elfouhaily et al*., [1997]. This model reproduces the Cox-Munk slope moments [*Cox and Munk*, 1954], and its development is based only on hydrodynamic properties of the sea surface. No tuning of the spectrum to obtain agreement with microwave scattering data has been done.

We write the 2-D sea surface spectrum in the form

$$y\left(\vec{k}\right) = S(k)n(k)\cos^{2s(k)}\left(\frac{f-f_w}{2}\right) \tag{10}$$

where the omni-directional spectrum, S(k), is a function of the magnitude of the surface-wave wavenumber, $\vec{k}$, and the cosine term describes the 2-D angular spreading properties. The angle f is the polar angle of the wavenumber vector $\vec{k}$, and f_w is the wind direction. The spectrum is defined such that

$$\int y\left(\vec{k}\right)d\vec{k} \equiv \int_0^\infty dk\,k\,n(k)S(k)\int_{-p}^{p} df\,\cos^{2s(k)}\left(\frac{f-f_w}{2}\right) \tag{11}$$

and n(k) is chosen as the reciprocal of the integral over the cosine term. With this normalization, the mean-squared height of the surface, $\left\langle h^2\right\rangle$, and the second-order slope moments, $\left\langle s_i s_j\right\rangle$ are given by

$$\left\langle h^2\right\rangle = \int_0^\infty S(k)k\,dk \tag{12a}$$

$$\begin{aligned}
\left\langle s_x{}^2\right\rangle &= \int_0^\infty S(k)k\,dk\int_{-p}^{p}\Phi(k,f-f_w)\cos f\,df,\\
\left\langle s_y{}^2\right\rangle &= \int_0^\infty S(k)k\,dk\int_{-p}^{p}\Phi(k,f-f_w)\sin f\,df,\\
\left\langle s_x s_y\right\rangle &= \int_0^\infty S(k)k\,dk\int_{-p}^{p}\Phi(k,f-f_w)\cos f\sin f\,df.
\end{aligned} \tag{12b}$$

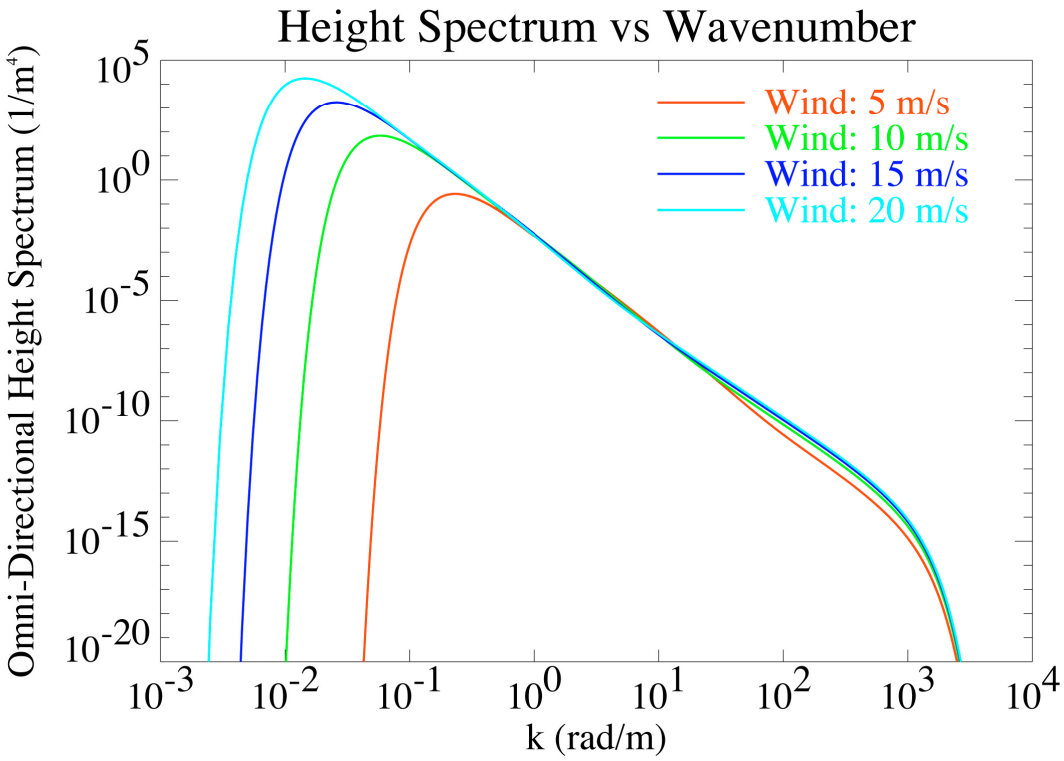

Figure 4.3. Omni-directional surface wave spectrum versus wavenumber. The red, green, blue and cyan curves show the spectral density for wind speeds of 5, 10, 15, and 20 m s^{-1}, respectively.

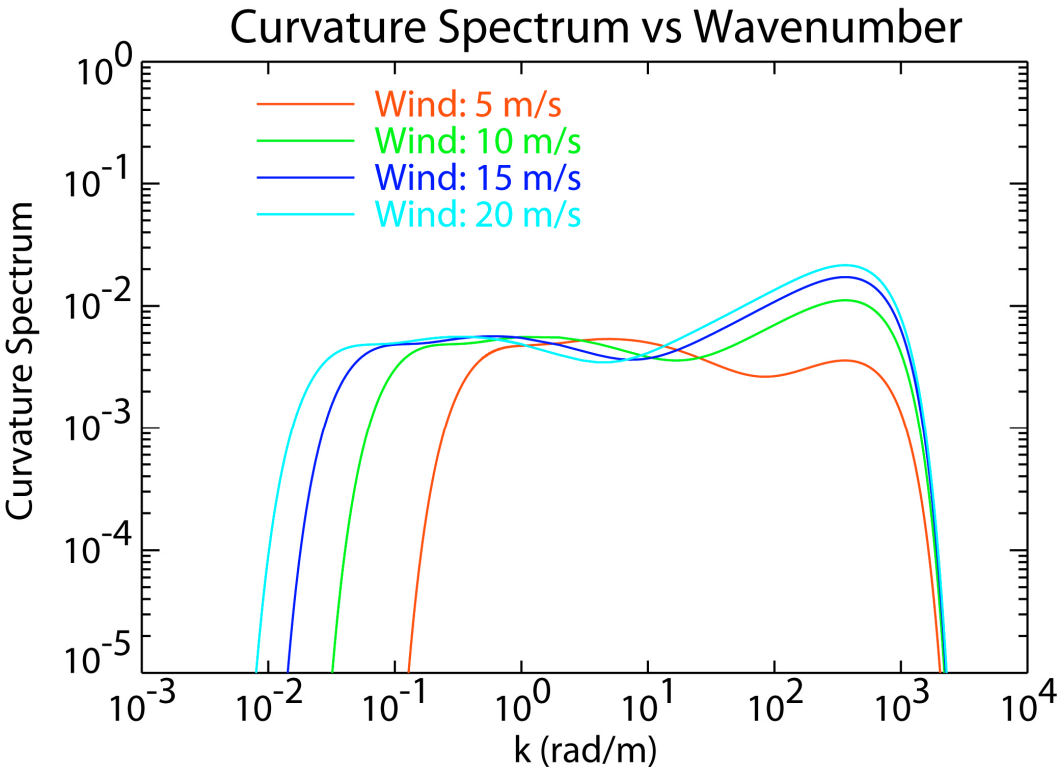

Figure 4.4. Surface wave curvature spectrum versus wavenumber. The red, green, blue and cyan curves show the spectrum for wind speeds of 5, 10, 15, and 20 m s^{-1}, respectively.

The red, green, blue, and cyan curves in Figure 4.3 show the behavior of S(k) as a function of k for wind speeds of *5, 10, 15*, and *20* m s^{-1}, respectively. One can see from this figure that the spectral peak occurs at lower wavenumbers as the wind speed increases and the spectral density of the dominant components increase with wind speed as one expects. This behavior is simply because stronger winds produce longer and higher waves. The dominant (peak) wavenumbers for the wind speeds of *5, 10, 15*, and *20* m s^{-1} plotted in Figure 4.3 correspond to wavelengths ($l = 2p/k$) or about 28 m, 114 m, 256 m, and 438 m, respectively. The power in these components is 10 or 15 orders of magnitude larger than that in the spectral region of the microwave Bragg waves (k~30 rad m^{-1} to 600 rad m^{-1} corresponding to λ~0.2 m to 0.01 m) which play an important role in microwave scattering.

An important, but not immediately apparent feature of the spectra plotted in Figure 4.3 is that in wavenumber region between about 1 and 10 rad m^{-1}, the spectra show very little wind speed dependence. This is the so-called equilibrium sub-range. Energy input at the high wavenumber end of this region is very nearly balanced by output at the low wavenumber end. One can therefore conclude by dimensional arguments that the spectral density in this region should be proportional to k^{-4} [*Phillips*, 1977]. It can be seen from Figure 4.3 that this dependence is indeed present. Based on our findings concerning the dependence of the NRCS on the surface spectrum as given in (8), we conclude that a radar whose wavenumber is less than about 10 rad m^{-1} (λ≈*0.6* m, ν≈*0.5* GHz) would not be a particularly good wind sensing device since the spectral components to which it would be sensitive have only a small wind speed dependence.

Figure 4.4 shows the wind dependence of the high wavenumber portion of the surface wave spectrum in a more convincing manner. In this figure, we have plotted the curvature spectrum; $k^4 S(k)$, versus k. As before, we show the results for a range of wind speeds from 5 to 20 m s^{-1}. The factor of k^4 in the curvature spectrum accentuates the high-wavenumber portion of *S(k),* and renders the equilibrium sub-range more or less independent of *k.* One can see immediately from Figure 4.4 that, aside from the low-wavenumber behavior associated with the decrease of the spectral peak position with increasing winds, the major wind-speed dependence is clearly concentrated in the wavenumber band between about 30 and 700 rad m^{-1} (wavelengths of *0.2* to *.009* m). The peak sensitivity to changes in wind speed appears to occur at a *k*-value of about 300 rad m^{-1} (λ≈*0.02* m). Since surface waves in this wavenumber band are the slowest moving waves on the surface, initial energy input from the wind occurs at these wavenumbers; hence the high sensitivity to wind fluctuations. This sensitivity is well known to yacht skippers who look for local patches of small-scale ripples (cats' paws) on the sea surface to assess wind conditions. In fact, many microwave scatterometer satellite platforms, including QuikScat (launched by NASA in June 1999) [*Spencer et al*., 2000], operate at K_u-band (ν≈*15* GHz) corresponding to a *0.02* m wavelength to take advantage of this wind-speed sensitivity to produce estimates of the near-surface wind field over the world's oceans.

Up to now, we've concentrated on the wind dependence of the omni-directional factor, *S(k)*, in the expression for the 2-D surface wave spectrum in (10). We now want to examine the form of the cosine term that determines the angular width of the spectrum. Note from the form of this term that the angular width is determined by the exponent *2s(k)* in (10). As this exponent becomes larger, the directionality of the corresponding wave component becomes more focused along the wind direction. This property is shown graphically in Figure 4.5 by polar plots of $n(k)\cos^{2s(k)}\left(\frac{f}{2}\right)$. The red, blue, green and cyan curves show this function for *k*-values of 0.25, 10, 100, and 1000 rad m^{-1}, respectively, and a wind speed of 10 m s^{-1}. Notice from the figure that the 0.25 rad m^{-1} ($l \approx 1.6$ m) curve is highly directional. The two crosswind spectral components

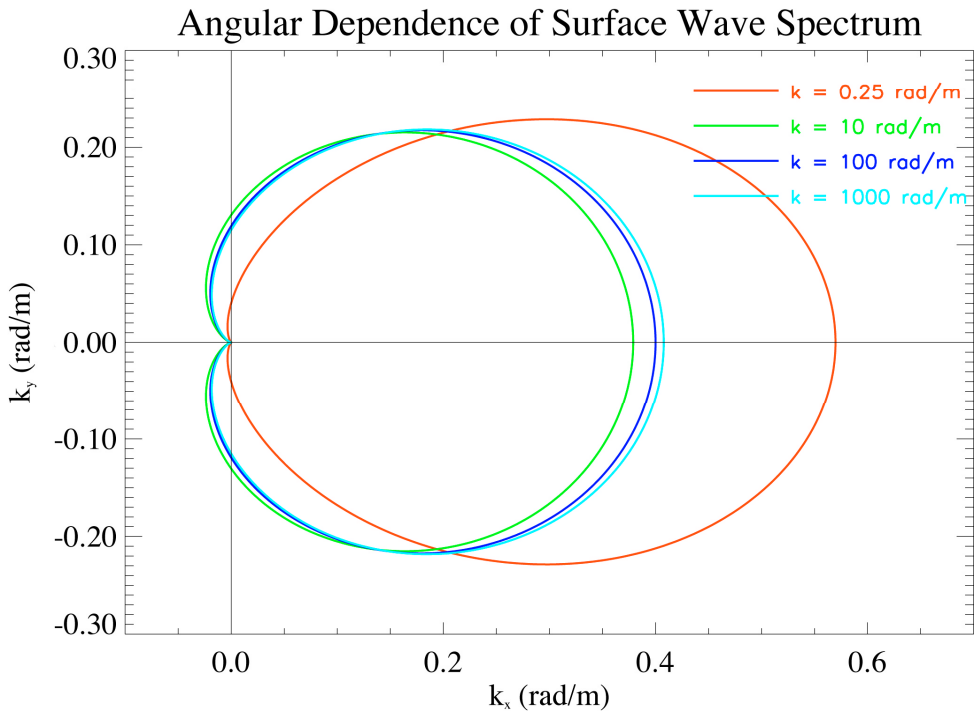

Figure 4.5. Polar plot showing the angular dependence of the surface wave spectrum. The red, blue, green and cyan colored curves show this function for *k*-values of *0.25, 10, 100*, and *1000* rad m^{-1}, respectively, and a wind speed of 10 m s^{-1}.

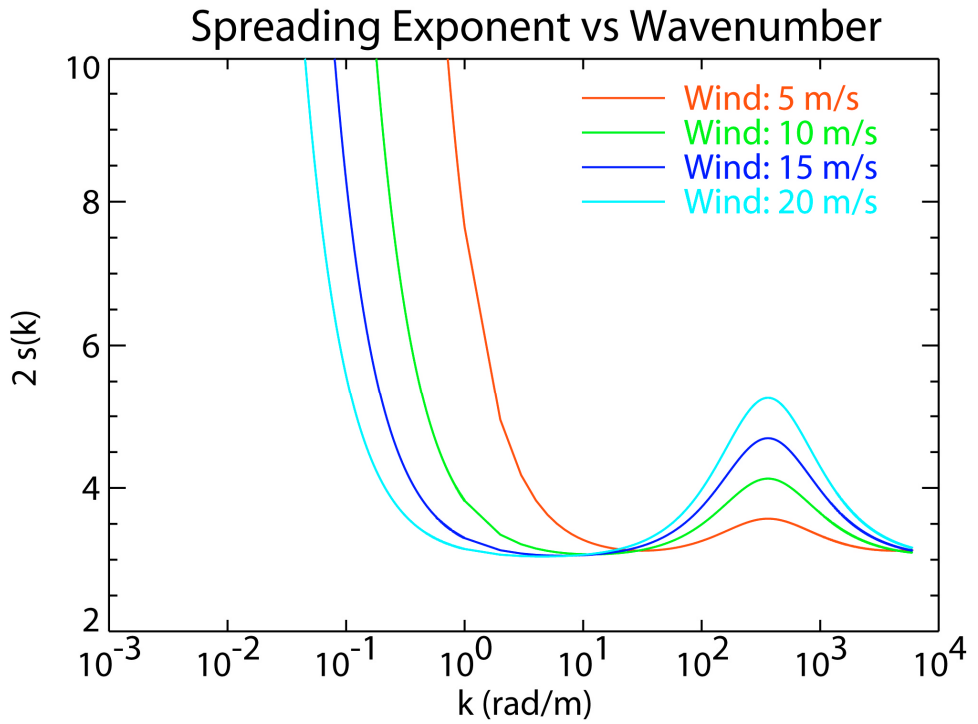

Figure 4.6. Plot showing the spreading exponent of the cosine term that describes the angular dependence of the surface wave spectrum. The red, blue, green and cyan colored curves show this exponent as a function of *k* for wind speeds of *5, 10, 15,* and *20* m s^{-1}, respectively.

(along the $\pm k_y$-directions) are roughly 10 times smaller than the along-wind component. The larger k-value components have about a 1:4 ratio of crosswind to along-wind spectral density. We also see from Figure 4.5 that for wavenumbers larger than 10 rad m^{-1} or so, the spectral components again become somewhat more directional. This effect is less pronounced for low winds, and is a result of the shorter waves being partially aligned in the direction of the longer wind waves (if they exit).

We can see more clearly how the angular dependence of the spectrum varies with wind speed by plotting the exponent of the cosine term in (10). Such a plot is shown in Figure 4.6 where wind speeds of *5, 10, 15,* and *20* m s^{-1} are shown by the red, blue, green and cyan curves, respectively. The large values of the spreading exponent (*2* s(k)) for small wavenumbers indicate the strong focusing of the longer waves. The broadest portion of the spectrum occurs for somewhat shorter waves in the equilibrium sub-range, and still shorter waves become more focused as the wind increases because of their alignment with the long waves. (The reader should be reminded here that the behavior of the spreading exponent shown in Figure 4.6 is based on a spectral model. Actual measurements of this and related quantities are difficult to collect, and error bounds tend to be large.)

With our discussion of the properties of the ocean surface wave spectrum complete, we are finally in a position to examine how microwave backscatter from the sea depends on environmental parameters (e.g., wind velocity) and radar geometry (e.g., incidence angle and look direction with respect to the wind vector).

4.3.4 Dependence of Ocean Backscatter NRCS on the Surface Wind Field

If a model of the ocean wave spectrum that gives a robust characterization of the surface behavior as a function of a set of environmental parameters is available, then one can, at least in principle, estimate these parameters from measurements of the backscatter NRCS of the sea. In Section 4.3.3, we examined the functional dependence of a particular spectral model on the near-surface wind vector. What we want to show in the present section, using the results of Section 4.3.3 as an example, is how backscatter NRCS measurements from the ocean surface can be used to estimate the surface wind. To proceed, we simply insert the example spectral model [*Elfouhaily et al*., 1997] from Section 4.3.3 into (8) and (9), and compute the resulting backscatter for the small-perturbation NRCS. The results of this computation are shown as a function of radar look direction (with respect to wind direction), f, for VV- and HH-polarization in the upper and lower panels of Figure 4.7, respectively. The results in both panels were computed for an incident angle $q=45°$ and a microwave wavelength of *0.02* m (K_u-band).

The panels in Figure 4.7 illustrate several important points concerning general properties of microwave backscatter from the sea surface. First, we see that the cross section, for any particular look direction or polarization state, increases with wind speed. This is because the corresponding (K_u-band) Bragg component of the surface wave spectrum also shows such wind dependence. (e.g., Figure 4.4 for $k»535$ rad m^{-1}.) Also, in the SPM limit shown here, the ratio between the HH-pol and VV-pol cross section (the polarization ratio) for fixed incident angle and look direction is simply the ratio of the $\left|G_S^{pq}(q)\right|^2$ terms evaluated for the relevant polarization states. In the SPM limit, this ratio depends only on the incident angle and equals about *10* dB for the case of interest here. One of the most important features illustrated by Figure 4.7 is the sinusoidal behavior of the NRCS as a function of f. In particular, one sees that the crosswind NRCS ($f=90°$) is significantly less than that for upwind or downwind looks ($f=0°$

or *180*°). The upwind to crosswind ratio increases with wind speed and is about *3* dB for a wind speed of *10* m s^{-1} at both polarizations. The difference between the upwind and crosswind NRCS (in the SPM limit) is caused by the (wind-dependent) spreading of the surface wave spectrum that we discussed in Section 4.3.3 and illustrated in Figures 4.5 and 4.6. Note also from Figure 4.7 that in the SPM limit, the upwind to downwind cross section ratio is unity. This will be discussed in more detail later.

Because of the sinusoidal behavior of the NRCS as shown in Figure 4.7, it is clear that one cannot uniquely specify the surface wind vector from a single NRCS measurement (even if one had complete confidence in the surface spectral model). This is because a particular NRCS value could result either from a particular wind vector aligned along the radar look direction or from another vector with a somewhat higher magnitude (speed), oriented at some (non-zero) angle to the radar look. Thus, measurements of the NRCS from a particular spot on the sea surface from different look directions (and a fixed incident angle) are required to uniquely specify the wind vector.

If the goal is to estimate the surface wind from measurements of microwave backscatter measurements from the sea surface, one might conclude at this point that the surface wave spectral model is not needed. This is partially true since one can simply collect backscatter measurements, for example from an airborne platform, over areas of the ocean where wind fields are available from *in situ* buoys or other independent sources. If a wide range of environmental conditions is sampled, one can use the database to determine an empirical relationship between the NRCS and the wind vector for each look direction and the desired range of incident angles. This is, in, fact the basis for present-day wind scatterometry where the results of this type of analyses has been extremely impressive. (For an overview of the topic of wind scatterometry, see e.g., *Atlas and Hoffman* [2000].) For the discussion in this chapter, we have introduced the surface wave spectrum in order to motivate the general physical ideas that govern the scattering physics. It is however interesting at this stage of our development to compare the very simple SPM scattering model with a commonly used scatterometer algorithm.

Scatterometer algorithms typically are written in the form

$$s_{pp}^{scatt} = aU^{g}\left\{1 + b\cos(f - f_w) + c\cos[2(f - f_w)]\right\} \tag{13}$$

where U is the wind speed, f is the radar look direction, f_w is the wind direction, and the wind-speed exponent $g > 0$. The parameters *a, b, c*, and g are generally functions of incident angle, radar frequency, and polarization. One can see from (13) that s_{pp}^{scatt} is symmetric about the wind direction, and for fixed f, is a monotonically increasing function of U. The functional form for the scatterometer algorithm given by (13) is more flexible than the expression of (8) and (9) for the NRCS in the SPM limit due to the presence of the $\cos(f - f_w)$.. This cosine term allows for a different cross section for upwind and downwind radar looks since such a difference is seen in the data. For moderate incident angles ($20^\circ \le q \le 60^\circ$), microwave scatterometer algorithms generally predict that the ratio of the upwind to crosswind cross section is around *3* dB, while the upwind-to-downwind ratio is more like 1 dB.

In Figure 4.8, we plot the NRCS from the SaSS-II algorithm, developed for use with the K_u-band *(l=0.02* m) scatterometer on board the SEASAT satellite [*Wentz et al.*, 1984], as a function of radar look direction for an incident angle of 45º. The solid blue curve shows the VV-pol results and the solid red curve shows the results for HH-pol. The red and blue dashed curves

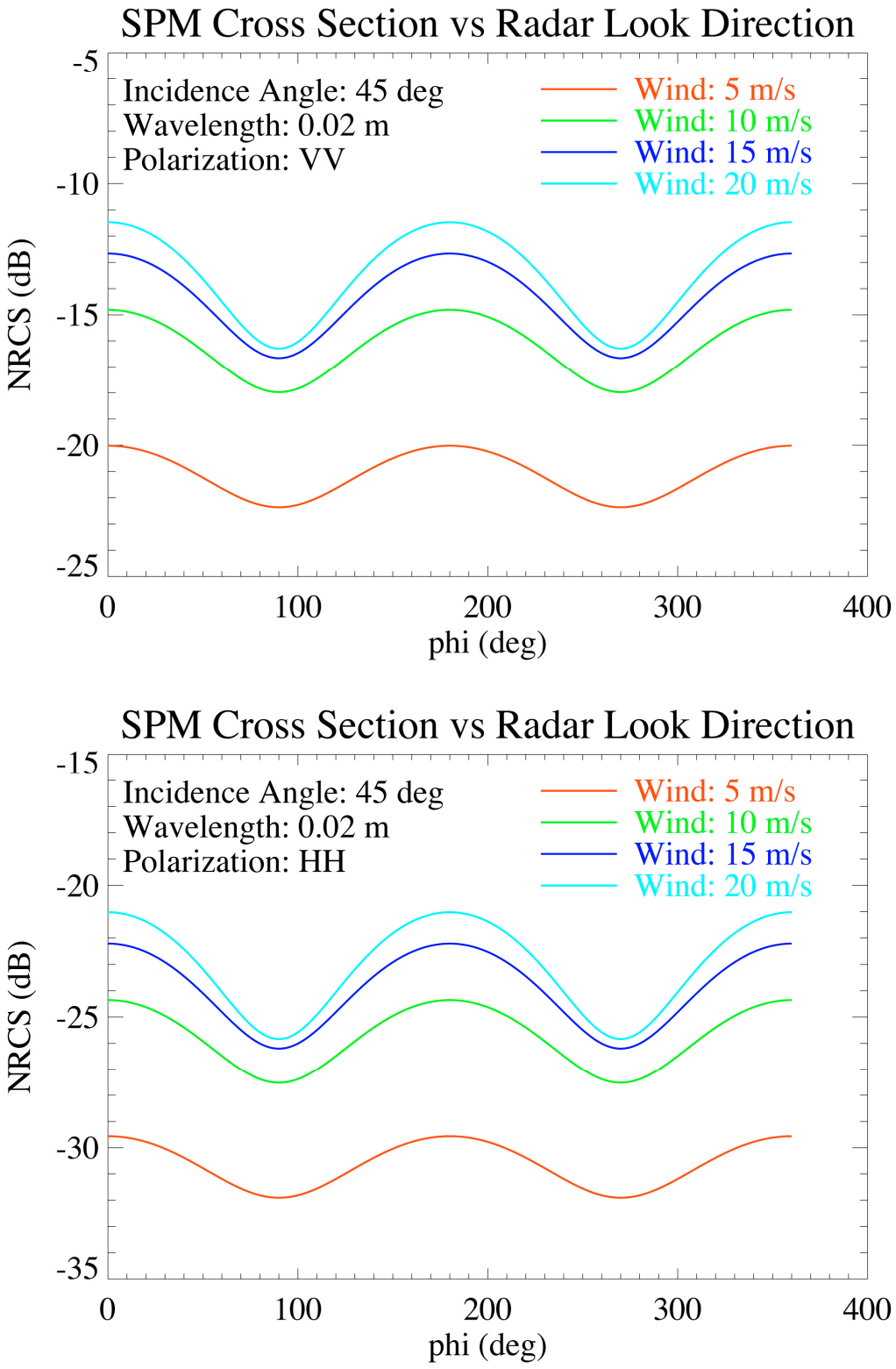

Figure 4.7. Small Perturbation (SPM) NRCS as a function of radar look direction, f, with respect to the wind direction for a radar wavelength of 0.02 m and an incident angle of 45º. Cross sections for wind speeds of *5, 10, 15*, and *20* m s^{-1} are shown by the red, green, blue, and cyan curves, respectively. The top panel shows the results for VV-polarization while the bottom panel is for HH-pol.

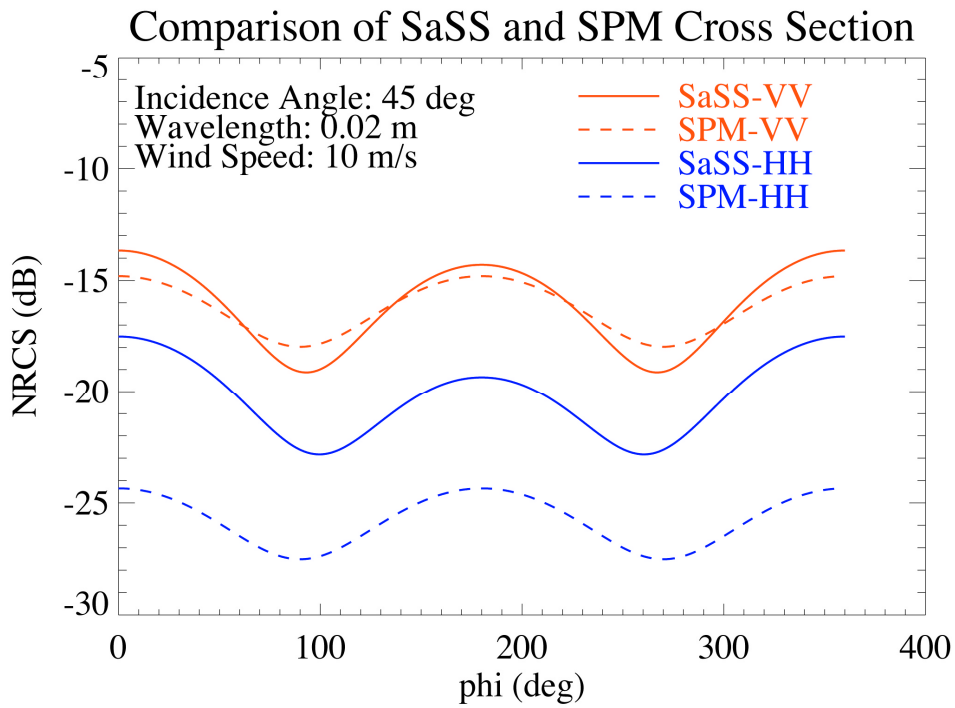

Figure 4.8. K_u-band NRCS at 45º incidence at VV- (blue curves) and HH-polarization (red curves) as a function of radar look direction. The solid curves show the NRCS computed with the empirical SaSS-II scatterometer algorithm and the dashed curves show the SPM results.

in Figure 4.8 show the corresponding NRCS values computed using the simple SPM model developed in Section 4.3.2. It is interesting that the NRCS computed for VV-pol using the SPM agrees reasonably well with that from the empirical SaSS-II algorithm. The mean levels are roughly the same for both methods, but the SPM slightly underestimates the upwind-to-crosswind ratio. The upwind-to-downwind ratio for VV-pol from the SaSS-II algorithm is about 1 dB, while the SPM predicts no difference between the upwind and downwind NRCS as we've seen before. For HH-pol , on the other hand, there is more than a 6 dB underestimate of the mean cross section by the SPM as well as an underestimate of the upwind-to-crosswind ratio similar to that found for VV-pol.

At this point, it should be mentioned that we have chosen to use the SaSS-II scatterometer algorithm in our discussion for illustrative purposes only. Since the development of SaSS-II in the mid 80's, other scatterometer algorithms have been developed for use at several microwave frequencies besides K_u-band. Of particular interest for this volume, is the C-band algorithm Cmod4 [*Stoffelen and Anderson*, 1997] widely used with the ERS-1/2 scatterometer, and more recently to extract high-resolution wind estimates from the ERS-1/2 and RADARSAT-1 SAR. This latter research is discussed by Monaldo and Beal in Chapter 13.

4.3.5 Refinements to Analytical Rough-Surface Scattering Models

As shown in Figure 4.8, a simple SPM prediction shows reasonable agreement at VV-pol with the NRCS predicted by the empirically derived SaSS-II scatterometer algorithm. At HH-pol, however, the agreement is much less satisfactory. This feature of the SPM can be explained qualitatively by at least two different physical processes occurring on the sea surface. The first process not explicitly accounted for in the SPM is that for realistic situations, the short-scale

Bragg waves responsible for the scattering are not propagating on a flat surface (as assumed in the SPM). Rather, these waves are propagating over the crests and troughs of the long-scale surface waves, and the local angle of incidence at each point along this path deviates from the vertical according to the local slope of the long-scale surface. This situation is the basis for the composite model, discussed earlier in Section 4.3.2, and is represented schematically in Figure 4.9. The arrows in Figure 4.9 represent the local normal to the long-wave surface (red curve) and indicate how the local angle of incidence, and hence the scattering from the short-scale waves (blue curve), can change along the long-wave surface. The SPM backscatter cross section, s_{pq}^{BSPM}, given by (8) and (9) is much more sensitive to changes in the incident angle, q, for HH-pol than for VV-pol. This means that the HH-pol NRCS is more sensitive to changes in the local incident angle produced by variations in the long-scale surface slope. Thus, if the effect of long-scale slope variation is not included in the description of the scattering process, one should expect that this omission would be more important for HH-pol scattering. The change in the NRCS of microwave backscatter from the sea surface due to the changing local incident angle is sometimes referred to as *tilt modulation*.

The backscatter cross section in composite-model type calculations, s_{pq}^{BCM}, may be written by weighting the SPM cross section expression given by (8) and (9) by the probability density function (PDF) of the in-plane and out-of-plane slope components s_x and s_y of surface waves longer than 3 or 4 times the Bragg wavelength *(l=2p//k_B)*. Schematically, this operation yields

$$s_{pq}^{BCM} = 4pk^2 \iint d\left[\vec{k}_B(s_x, s_y)\right] P(s_x, s_y) ds_x ds_y +$$

$$8pp^4 \iint \left| G_s^{pq}\left[?_l(s_x, s_y)\right]\right|^2 \left\{? \left[\vec{k}_{Bl}(s_x, s_y)\right] + ? \left[-\vec{k}_{Bl}(s_x, s_y)\right]\right\} P(s_x, s_y) ds_x ds_y \qquad (14)$$

where $P(s_x, s_y)$ is the surface slope PDF. The remaining terms in the integrand of (14) have the same meaning as those in (8) and (9) except that the incident angle, q, in those equations has been replaced by the local incident angle q_l. The slope dependence of q_l as well as that of k_B $(=2\, k_0 \sin q_l)$ on s_x and s_y is shown explicitly. The PDF is usually assumed to be Gaussian with a variance equal to the mean squared slope obtained from (the long-wave portion of) y at the wind speed in question. Physically, s_{pq}^{BCM} is simply computed from (14) by weighting the behavior of the simple SPM by the expected slope (tilt) of the long waves. The first term in (14) represents specular scattering, which now occurs whenever the local incident angle is zero, and generally dominates the scattering process out to incident angles of *20°* or so for typical microwave frequencies. For a Gaussian PDF, this term reduces to the familiar geometrical optics result [*Beckmann and Spizzichino*, 1963].

The second term in (14) represents the composite (or tilted) Bragg contribution, and is simply the average NRCS from the SPM model over the local incident angles chosen according to the long-scale slope PDF. As we have already discussed above, the SPM cross section, especially at H-pol, increases rapidly as the local incident angle decreases, so that the cross section predicted by (14) is larger than that predicted by the simple flat-surface SPM for both polarizations, with the HH-pol NRCS showing the largest percentage increase compared to the corresponding SPM result. Finally we should point out that in the composite model of (14), the polarization state of the incident field is referenced to the (tilted) local surface normal rather than

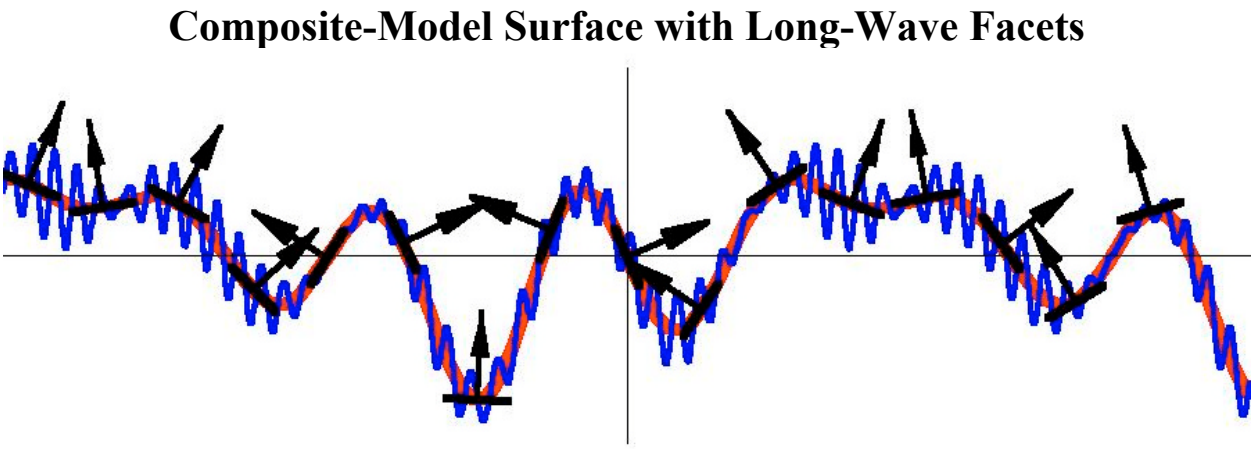

Figure 4.9. Schematic of composite-model surface. The red curve represents the long wave portion while the blue curves show the short-scale waves that propagate over this surface. The changing local angle of incidence over the long-wave surface is illustrated by linear facets whose normal vector is shown by the arrows.

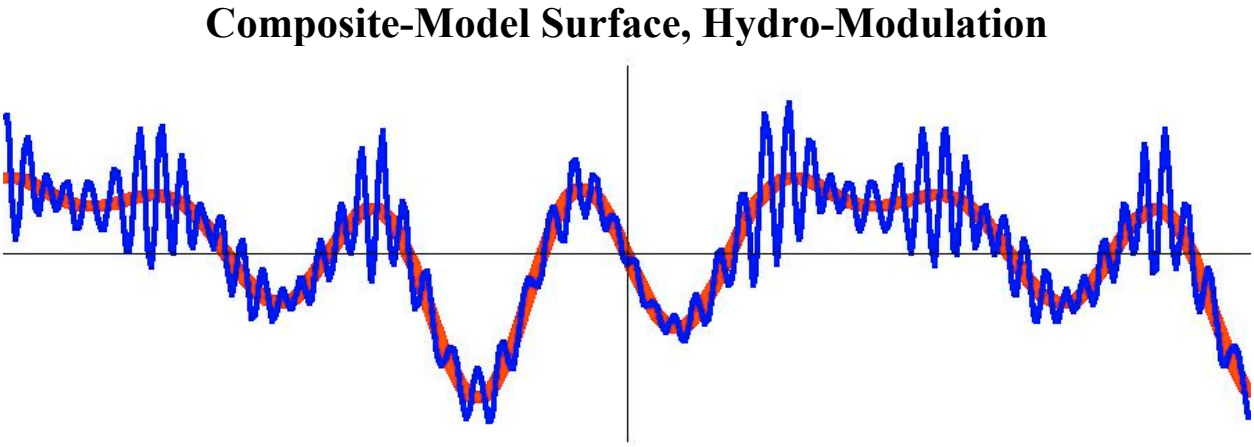

Figure 4.10. Schematic of the effect of hydrodynamic modulation on a composite-model surface. The amplitude of the short-scale roughness (blue curve) is enhanced near the crests of the long-wave surface (red curve).

to a fixed vertical direction. A vertically polarized incident field (referenced to a fixed coordinate system), for example, will generally have a small horizontally-polarized component when referenced to the local surface normal. Thus, unlike the case for the simple SPM, depolarization (i.e., the polarization state of the received field different from that of the incident field) can occur in the composite model due to out-of-plane tilting of the scattering surface. We represent this in (14) by the *pq* subscripts on s_{pq}^{BCM} rather than *pp* on s_{pp}^{BSPM} in (8). For further discussion of tilt modulation in composite model calculations, see e.g., *Thompson* [1989] and references contained therein.

There is another mechanism that can cause the observed backscatter cross section from the sea to be larger than the NRCS predicted by the SPM. This mechanism is related not so much to a deficiency in the description of the scattering physics in the SPM, but rather to the assumption that the height statistics of the scattering surface may be described as a two-point correlated Gaussian random process. (See the discussion in Section 4.3.2.) This assumption implies that the surface height autocorrelation function depends only on the separation distance

of the two points where the height is being correlated, and does not depend on the surface location where the autocorrelation is computed. Under these conditions, the surface is said to be homogeneous. The assumption of Gaussian height statistics further implies that the surface-wave field is linear. That is, the surface may be described as a linear combination of statistically independent sinusoidal (Fourier) components whose amplitudes are related to the components of surface wave spectrum y.

Although in many analyses of microwave scattering the assumption of Gaussian height statistics is present (explicitly or sometimes implicitly), the tendency for ocean waves to have rougher crests and smoother troughs than predicted by a Gaussian height distribution has been known for many years. (See, for example, the discussion in *Phillips* [1977].) One of the reasons for the non-Gaussian behavior of the ocean surface is the nonlinear nature of the equations that describe the free-surface boundary conditions that the wave field must satisfy [*Johnson*, 1997]. Other processes that affect the shape and evolution of the sea surface are energy input by the wind, dissipation of energy by breaking waves, and spectral modulation by variable surface current fields. For a detailed discussion of these and other processes important for understanding the behavior of surface waves, see *Komen et al*. [1994]. The upwind-to-downwind NRCS ratio observed in the scatterometer algorithms discussed in Section 4.3.4 is a result of the nonlinear nature of ocean surface waves. In particular, a non-zero, upwind-to-downwind NRCS ratio is due to the fact that the front (downwind) face of a sea surface wave tends to be rougher than the back face.

One of the most common mechanisms used to estimate the non-Gaussian behavior of the surface wave height distribution is through the modulation of the short-scale spectral density by the orbital currents associated with the long-wave surface. This modulation can be computed quantitatively using an action-balance formulation [*Plant*, 1990; *Thompson and Gotwols*, 1994], and usually predicts enhanced roughness near the crest and on the front (downwind face) of long-scale surface waves. In the spirit of the composite model, we schematically illustrate such spectral modulation in Figure 4.9 where one can see that the short-wave roughness (blue curve) is enhanced near the crests of the long-wave surface (red curve). This variable short-scale roughness will cause a modulation in the NRCS measured by a small-footprint radar over the long-wave phase. Such change in the NRCS of microwave backscatter from the sea surface due to spectral modulation of the short-scale waves induced by orbital currents associated with the long-wave surface is sometimes referred to as *hydrodynamic modulation*. Since it affects the magnitude of the short-wave spectral density, one can see from (14) that hydrodynamic modulation generally causes a similar increase in the NRCS for both VV- and HH-polarization. For HH-pol however, interference between tilt and hydrodynamic modulation is a strong function of radar look direction with positive interference for waves traveling toward the radar and negative interference for the opposite case. Therefore, researchers studying hydrodynamic modulation at intermediate angles of incidence (between approximately 20° and 60°) usually work at VV-pol where tilt modulation is small and the effect of hydro-modulation is maximized.

4.4. Remaining Problems and Future Directions

In recent years, it has become apparent that for incident angles greater than 25° or so, the difference between the measured polarization ratio (HH/VV) is greater than that predicted by standard composite-type scattering models. This under-prediction is generally larger for higher microwave frequencies, and becomes larger as the incident angle increases [*Thompson et al*., 1998]. Even relatively sophisticated models that include the tilt- and hydrodynamic-modulation

effects discussed above [*Romeiser et al*., 1997] generally cannot produce a large enough HH-pol NRCS to obtain agreement with experiment. We believe that this discrepancy may be at least partially explained by a more exact treatment of the non-linear nature of the ocean surface waves. This non-linearity is manifest not only in the non-uniform distribution of short-scale roughness over the long-scale surface discussed above, but also in the shape of the long-scale surface itself. Therefore, many commonly used models of the hydrodynamic modulation process, which assume that the short-scale roughness variation is proportional to a linear long-wave surface, do not capture all of the features in the inherently nonlinear process. We have recently shown that such features can have a significant influence on the surface statistics [*Elfouhaily et al.,* 2001b]. This influence is most evident in microwave backscattering at high incident angles (greater than 70° or so). For this geometry, higher than usual wave crests resulting from nonlinear surface statistics are more effective scatterers (especially at HH-pol) than for lower incident angles where microwave backscatter is not so sensitive to small changes in crest height resulting from the nonlinearities. Much of the current research in rough-surface scattering is focused on understanding the differences between measurement and theoretical predictions of the backscatter cross section at high incident (low grazing) angles. (For a survey of some of this research see, e.g., the articles in the *IEEE* special issue on low grazing-angle scattering edited by *G.S. Brown* [1998].)

As alluded to in the preceding paragraph, the treatment of nonlinearities inherent in surface wave hydrodynamics leads to a scale separation reminiscent of that encountered in the derivation of the composite model for microwave scattering. It is important to keep in mind, however, that the separation wavenumber, k_c, for these two situations is quite different. The separation wavenumber for hydrodynamics corresponds to a wavelength of a few meters or so [*Elfouhaily et al.,* 2001b], while that required in the composite model for microwave scattering corresponds to several Bragg wavelengths; on the order of at most a few tens of centimeters depending on the specific radar frequency. Fortunately, as discussed in Section 4.3.1, a reasonably accurate analytic model, for which an electromagnetic scale separation is not required, already exists [*Elfouhaily et al.*, 1999]. We can therefore formulate a new hydrodynamic composite-type model using the same philosophy as that used to write (14). In our new composite model, we replace the expression for the SPM cross section used in (14) by that for the analytic model [*Elfouhaily et al.*, 1999] defined by (1) through (4) with the incident angle implicit in these equations now being the local angle of incidence referenced to the long-(hydrodynamic) scale surface. Note for this new formulation, there is only one term in the integrand. The specular term in (14) is already accounted for in the analytic model. Also following the previous development, the slope PDF appearing in (14) would be for the long-hydro-scale surface and in particular would not need to be Gaussian. In this way, the new model would include tilt modulation from the nonlinear long-scale surface. Hydrodynamic modulation of the short-scale spectrum could be included, for example, as outlined in *Elfouhaily et al.* [2001b]. Also as outlined in this reference, the formulation of the polarization dependence of the analytic model in terms of coordinate-independent vectors greatly simplifies the required transformations to local coordinate system. At the time of this writing, development of a nonlinear surface scattering simulation of the type discussed here is underway. In addition to the NRCS, this simulation will also predict the local Doppler spectra of the scattered field based on the general ideas discussed in *Thompson* [1989]. Knowledge of the Doppler spectra is required, for example, in the remote sensing of ocean surface currents [*Thompson et al*., 1991].

4.5. Conclusion

In this chapter, we have presented a general discussion of the basic physics that must be included in any quantitative description of microwave scattering from the sea. We have attempted to highlight general concepts with simplified descriptions for the non-specialist, but have also included numerous references for those who may be interested in more technical details. It is clear that an understanding of the relationship between the scattered field and the scattering surface at a fundamental level is a necessity for the proper interpretation of existing remote sensing data as well as the efficient implementation of future ocean remote-sensing techniques.

Although the examples in this chapter are concentrated mainly on scatterometry applications, the basic physics is applicable to other microwave sensors (both active and passive) including altimeters [*Fu and Cazenave*, 2001] and passive microwave radiometers [*Ulaby et al*., 1982]. A useful discussion of these and other remote sensing instruments for oceanographic applications is given in chapter 8 of *Apel* [1987]. Perhaps most important, at least for the present volume is that the scattering physics discussed in this chapter applies directly to microwave SAR imaging of the sea surface.

We hope, as readers proceed to chapters in the remainder of this volume discussing applications of synthetic aperture radar for the imaging of coastal internal waves or the production of high-resolution wind field maps using many of the scatterometry techniques discussed above, they will recall the description of microwave scattering in this chapter. If they do this, they will realize that the internal waves are apparent in the imagery essentially because the orbital motion associated with these waves modulates the short-scale surface waves to produce alternating rough and smooth regions over the internal wave phase (hydro-modulation). As we have seen, this roughness modulation can produce a corresponding modulation in the NRCS, and thus render the internal waves visible in the imagery. Likewise, variability in the strength of the surface wind field will modulate the spectral density of short-scale surface waves, again producing modulation in the imagery characteristic of the boundary-layer wind field. In this way, the basic scattering physics reviewed in this chapter should assist readers not only to understand but also to assess the validity and accuracy of the various applications discussed later on in the volume.

4.6 References

Apel, J. R., 1987: *Principles of Ocean Physics.* Academic Press, 634 pp.

——, 1994: An improved model of the ocean surface wave vector spectrum and its effects on radar backscatter. *J. Geophys. Res*., **99**, 16 269–16 291.

Atlas, R., and R. N. Hoffman, 2000: The use of satellite surface wind data to improve weather analysis and forecasting at the NASA Data Assimilation Office. *Satellites, Oceanography and Society*, David Halpern, Ed., Elsevier Oceanography Series, Vol. 68, Elsevier, 57–79.

Beckmann, P., and S. Spizzichino, 1963: *The Scattering of Electromagnetic Waves from Rough Surfaces*. Macmillan, 503 pp.

Bjerkaas, A. W., and F. W. Riedel, 1979: Proposed model for the elevation spectra of a wind-roughened sea surface. Applied Physics Laboratory, Johns Hopkins University Tech. Rep. APL-TG-1328-I-31, Laurel, MD, 31 pp.

Brown, G. S., Ed., 1998: Special issue on low grazing-angle scattering. *IEEE Trans. Antennas Propag.,* **46**, 164 pp.

Cox, C. S., and W. H. Munk, 1954: Statistics of the sea surface derived from sun glitter. *J. Mar. Res*., **13**, 198–227.

Donelan, M. A., and W. J. P. Pierson, 1987: Radar scattering and equilibrium ranges in wind-generated waves with applications to scatterometry. *J. Geophys. Res*., **92**, 4971–5029.

Elfouhaily, T., B. Chapron, K. Katsaros, and D. Vandemark, 1997: A unified directional spectrum for long and short wind-driven waves. *J. Geophys. Res*., **102**, 15 781–15 796.

——, D. R. Thompson, D. Vandemark, and B. Chapron, 1999: A new bistatic model for electromagnetic scattering from perfectly-conducting random surfaces. *Waves Random Media,* **9**, 281–294.

——, ——, D. E. Freund, D. Vandemark, and B. Chapron, 2001a: A new bistatic model for electromagnetic scattering from perfectly-conducting random surfaces: Numerical evaluation and comparison with SPM. *Waves Random Media,* **11**, 33–43.

——, ——, D. Vandemark, and B. Chapron, 2001b: Higher-order hydrodynamic modulation: Theory and applications for ocean waves. *Proc. Roy. Soc. Math. Phys. Eng. Trans.*, in press.

Fu, L. L., and A. Cazenave, 2001: *Satellite Altimetry and Earth Science*. Academic Press, 463 pp.

Fung, A. K., 1994: *Microwave Scattering and Emission Models and their Applications*. Artech House, 573 pp.

Jackson, J. D., 1997: *Classical Electrodynamics*. 3d. ed. John Wiley & Sons, 808 pp.

Johnson, R. S., 1997: *A Modern Introduction to the Mathematical Theory of Water Waves*. Cambridge University Press, 445 pp.

Komen, G. J., L. Cavaleri, M. Donelan, K. Hasselmann, S. Hasselmann, and P. A. E. M. Janssen, 1994: *Dynamics and Modeling of Ocean Waves*. Cambridge University Press, 532 pp.

Phillips, O. M., 1977: *The Dynamics of the Upper Ocean.* Cambridge University Press, 336 pp.

Plant, W. J., 1990: Bragg scattering of electromagnetic waves from the air/sea interface. *Surfaces Waves and Fluxes.* G. L. Geerneart and W. J. Plant, Eds., Vol. 2, Kluwer Academic, 41–108.

Romeiser, R., W. Alpers, and V. Wismann, 1997: An improved composite surface model for the radar backscattering cross section of the ocean surface. 1: Theory of the model and optimization/validation by scatterometer data. *J. Geophys. Res*., **102**, 25 237–25 250.

Spencer, M. W., C. Wu, and D. Long, 2000: Improved resolution backscatter measurements with the SeaWinds pencil-beam scatterometer. *IEEE Trans. Geosci. Remote Sens,* **38**, 89–104.

Stoffelen, A., and D. Anderson, 1997: Scatterometer data interpretation: Measurement space and inversion. *J. Atmos. Oceanic Technol.,* **14**, 1298–1313.

Thompson, D. R., 1989: Calculation of microwave Doppler spectra from the ocean surface with a time-dependent composite model. *Radar Scattering from Modulated Wind Waves*, G. J. Komen and W. A. Oost, Eds., Kluwer Academic, 27–40.

Thompson, D. R., and B. L. Gotwols, 1994: Comparisons of model predictions for radar backscatter amplitude probability density functions with measurements from SAXON. *J. Geophys. Res*., **99**, 9725–9739.

Thompson, D. R., B. L. Gotwols, and W. C. Keller, 1991: A comparison of K_u-band Doppler measurements at 20° incidence with predictions from a time-dependent scattering model. *J. Geophys. Res.,* **96,** 4947–4955.

Thompson, D. R., T. M. Elfouhaily, and B. Chapron, 1998: Polarization ratio for microwave backscattering from the ocean surface at low to moderate incidence angles. *Proc. IGARSS'98*, Seattle, WA, IEEE, 1671–1673.

Ulaby, F. T., R. K. Moore, and A. K. Fung, 1982: *Microwave Remote Sensing: Active and Passive.* Vol. 2. Addison-Wesley, 608 pp.

Voronovich, A. G., 1994: *Wave Scattering from Rough Surfaces*. 2d ed. Springer Verlag, 228 pp.

Wentz, F. J., S. Peterheruch, and L. A. Thomas, 1984: A model for ocean radar cross section at 14.6 GHz. *J. Geophys. Res*., **89**, 3689–3704.